

# **Towards Posture-Dependent Human Pulmonary Oxygen Mapping using Hyperpolarized Helium and an Open-Access MRI System**

R. W. Mair<sup>1</sup>, L. L. Tsai<sup>1,2,3</sup>, C.-H. Li<sup>1,4</sup>, M. J. Barlow<sup>5</sup>, R. Scheidegger<sup>1,2</sup>,  
M. S. Rosen<sup>1,4</sup>, S. Patz<sup>3,6</sup> and R. L. Walsworth<sup>1,4</sup>

<sup>1</sup> Harvard-Smithsonian Center for Astrophysics, Cambridge, MA 02138, USA.

<sup>2</sup> Harvard-MIT Division of Health Sciences and Technology, Cambridge, MA 02139, USA.

<sup>3</sup> Harvard Medical School, Boston, MA 02115, USA.

<sup>4</sup> Department of Physics, Harvard University, Cambridge, MA 02138, USA.

<sup>5</sup> Sir Peter Mansfield MRI Center, University of Nottingham, Nottingham, UK.

<sup>6</sup> Department of Radiology, Brigham And Women's Hospital, Boston, MA 02115, USA.

## **Corresponding Author:**

Ross Mair

Harvard Smithsonian Center for Astrophysics,

60 Garden St, MS 59,

Cambridge, MA, 02138,

USA

Phone: 1-617-495 7218

Fax: 1-617-496 7690

Email: [rmair@cfa.harvard.edu](mailto:rmair@cfa.harvard.edu)

## INTRODUCTION

In recent years, MRI of inhaled, hyperpolarized  $^3\text{He}$  gas [1,2] has emerged as a powerful method for studying lung structure and function [3,4]. This technique has been used to make quantitative maps of human ventilation [5], obtain regional acinar structural information via measurements of the  $^3\text{He}$  Apparent Diffusion Coefficient (ADC) [6], and to monitor the regional  $\text{O}_2$  concentration ( $p_{\text{AO}_2}$ ) via the  $^3\text{He}$  spin-relaxation rate [7,8]. These techniques have applications to basic pulmonary physiology [9] as well as lung diseases such as asthma and emphysema [9,10].

Despite its clinical utility, all subjects undergoing lung imaging in a traditional clinical MRI scanner must lie horizontally – a consequence of the magnet design. Similar restrictions are imposed on subjects being studied by other clinical imaging modalities such as CT and PET. However, body orientation and postural changes have a significant effect on pulmonary function – much more so than any other body organ, and hence studies of pulmonary function at variable postures could have significant impact on both pulmonary physiology and medicine. For example, the regional distribution of pulmonary perfusion and ventilation have been a source of renewed interest in recent years [11-14], due to significant questions relating to the care and survival of patients with severe lung diseases such as acute respiratory distress syndrome [13].

Some initial studies with hyperpolarized  $^3\text{He}$  have shown that posture changes, even while horizontal, affect the lung structure modestly in a way that can nonetheless be clearly probed by  $^3\text{He}$  MRI [15]. To enable complete posture-dependent lung imaging, we have developed an open-access MRI system based on a simple electromagnet design that operates at a field strength  $\sim 200$  times lower than a traditional clinical MRI scanner [16,17]. To perform MRI at such a field strength, we exploit the practicality of hyperpolarized  $^3\text{He}$  MRI at magnetic fields  $< 10$  mT

[18-21].  $^3\text{He}$  hyperpolarized to 30–60% can be created by one of two laser-based optical pumping processes [1,2] prior to the MRI procedure; and then high-resolution gas space imaging can be performed without the need of a large applied magnetic field. Such high spin polarization gives  $^3\text{He}$  gas a magnetization density similar to that of water in  $\sim 10$  T fields, despite the drastically lower spin density of the gas.

We have previously described in detail the clinical motivation for posture-dependent pulmonary studies [16], and the design and operation of our imager [17]. In this chapter, we report progress towards posture-dependent functional human lung imaging: i.e., mapping regional pulmonary  $\text{O}_2$  partial pressure. Such experiments require higher  $^3\text{He}$  hyperpolarization than that required for simple spin-density imaging. We outline recent improvements to our  $^3\text{He}$  hyperpolarization apparatus, quantitative testing of the oxygen-mapping procedure using phantoms, and initial human  $p_{\text{A}}\text{O}_2$  maps using our open-access MRI system.

## EXPERIMENTAL

*Imager Design:* A detailed description of the design and operation of our open-access human MRI system is presented elsewhere [17]. Here, we provide a brief overview of the system.

The imager operates at an applied static magnetic field,  $B_0 = 6.5$  mT (65 G). This field is created by a four-coil, bi-planar magnet design [22] with pairs of coils measuring 2 and 0.55 m in diameter, separated by  $\sim 80$  cm. All four coils are powered by a single DC power supply with 42.2 A of current to reach the desired field of 6.5 mT, allowing  $^3\text{He}$  MRI at a frequency of 210 kHz. After shimming, the  $B_0$  field exhibits a total variation of less than  $\sim 5$   $\mu\text{T}$  (0.05 G) across the volume of a human chest. The resulting  $^3\text{He}$  NMR signals from such volumes exhibit spectral FWHM line-widths of  $\sim 30$  Hz.

We built planar gradient coils for the imager, thereby eliminating another restrictive cylindrical geometry found in clinical MRI scanners. The coils were designed to allow the acquisition of  $256 \times 256$   $^3\text{He}$  images across a 40 cm field of view (FOV) with an imaging bandwidth of 10 kHz, while avoiding noticeable concomitant field effects [23]. The coils are coplanar with each  $B_0$  magnet coil, maintaining the  $\sim 80$  cm spacing for subject access. The gradient coils are powered by Techron 8607 gradient amplifiers, and at maximum current, the three gradients each provide  $\sim 0.07$  G/cm gradient strength.

RF-frequency and gradient control is accomplished using a Tecmag Apollo MRI console, which operates at a frequency of 210 kHz without hardware modification. RF pulses are fed to a Communications Power Corp. Inc. NMR Plus 5LF300S amplifier, which provides up to 300 W of RF power. We use a single RF coil for  $B_1$  transmission and detection, in conjunction with a probe interface-T/R switch optimized for 200 kHz operation. The RF coil is a large solenoid  $\sim 50$  cm in diameter and length, that accommodates the subject's shoulders and arms, and completely covers their chest. Being a solenoid, the coil has very high  $B_1$  homogeneity [17], and can be rotated along with the subject in the imaging plane, while remaining perpendicular to the direction of  $B_0$ . The coil has a quality factor  $Q \sim 30$ , implying operating bandwidths of  $\sim 10$  kHz at the  $^3\text{He}$  Larmor frequency of 210 kHz.

To improve SNR, the  $B_0$ , gradient and  $B_1$  coils were housed inside an RF shielded room [Lindgren RF Enclosures] that attenuates environmental RF interference above 10 kHz by up to 100 dB. Power lines for the  $B_0$  magnet, preamplifier and RF coil connections all pass through commercial filters that shield out noise above 10 kHz. The gradient lines pass into the shielded room via three sets of custom high-current passive line filters that produce  $\sim 25$  dB attenuation at 100 kHz. The complete imager system, demonstrating subject access, is shown in **Figure 1**.

***Hyperpolarized  $^3\text{He}$  Production and Delivery:*** Hyperpolarized  $^3\text{He}$  gas is produced via the spin-exchange optical pumping (SEOP) technique using vaporized Rb as an intermediate [1]. Our modular  $^3\text{He}$  polarization apparatus [20] is located adjacent to, but outside, the RF shielded room. A magnetic field of 2.3 mT provides a quantization axis for optical pumping and prevents rapid polarization decay. It also provides a homogeneous  $B_0$  field for in-situ polarization monitoring using a bench-top Magritek Aurora spectrometer. For each experiment, we filled a  $\sim 80\text{ cm}^3$  Pyrex-glass polarization cell with  $\sim 5 - 6$  bar of  $^3\text{He}$  and 0.1 bar of  $\text{N}_2$ . The cell is heated to  $> 170^\circ\text{C}$ , and  $\sim 30\text{ W}$  of circularly polarized light at 794.7 nm is applied. After optical pumping for  $\sim 8 - 10$  hours, the  $^3\text{He}$  nuclear spin polarization reaches  $\sim 20 - 30\%$ . We then expand the polarized gas from the optical pumping cell into an evacuated glass chamber with a Teflon piston, which enables delivery of the  $^3\text{He}$  via Teflon tubing through a feed-through in the RF shielded room, either directly to a phantom, or to a delivery manifold adjacent to a human subject.

A significant limitation of the SEOP method is the slow production rate of hyperpolarized  $^3\text{He}$ . The demands for higher  $^3\text{He}$  polarization levels required for  $p\text{O}_2$  mapping experiments, and for higher volumes of hyperpolarized  $^3\text{He}$  for administration to human subjects in a timely manner has necessitated a number of modifications to the polarizer hardware, which we describe below.

The slow production rate of hyperpolarized  $^3\text{He}$  is the result of a small spin-exchange collision coefficient between Rb and  $^3\text{He}$ ,  $\sim 6.8 \times 10^{-20}\text{ cm}^3/\text{s}$ . Operating the SEOP cell at higher temperatures dramatically increases the vaporized Rb density in the cell, and hence the Rb- $^3\text{He}$  spin-exchange rate. However, the laser must provide sufficient resonant light in order to fully polarize the vaporized Rb at this higher density, otherwise the  $^3\text{He}$  polarization level will actually decrease as unpolarized Rb atoms collide with, and depolarize,  $^3\text{He}$  atoms. Although the current generation of Laser Diode Arrays (LDA) commonly used for SEOP may be rated at 60 W or

higher, their optical spectra are broad, with the desired wavelength of 794.7 nm generally appearing as a broad peak of  $\sim 3$  nm width (See **Figure 2**). As a result, relatively little of the rated laser power is actually resonant for the Rb polarization transition, making higher  $^3\text{He}$  spin polarization levels or production rates difficult to obtain without lasers of enormous power.

A concerted effort has taken place in recent years to attempt to narrow the laser spectral output, with the aim of making most of the laser light resonant for Rb polarization. Much of this work initially involved the use of significant amounts of additional optical hardware and an optical table (external cavity approach) [24]. A much simpler option, and one that can be easily integrated with standard LDA's, has emerged in the last year with the advent of Volume Holographic Gratings (VHG) [25]. These gratings can be used in an optical mount in front of a bare laser diode bar, or incorporated directly in LDA modules by laser manufacturers, and result in a resonant line of  $\sim 0.2 - 0.3$  nm FWHM. The VHG's self-seed the laser to provide a narrow resonant line output with only minimal laser power reduction. We have trialed two prototype commercial, fiber-coupled, VHG-narrowed 30 W LDA modules (Comet<sup>TM</sup>, under development by Spectra-Physics, Newport Corp., Tuscon, AZ).

The Comet module is also the first LDA system with power  $> 10$  W that has employed a polarization preserving fiber. Therefore, the laser output emerges from the fiber retaining  $> 90\%$  of its linear polarization, in a single beam that can be easily matched to the diameter of the polarization cell, and aligned parallel to the cell. This development further increases the amount of resonant light on the optical pumping cell over the traditional fiber-coupled LDA's that required additional optical polarization hardware and resulted in two non-parallel beams incident on the optical pumping cell [1,3]. Relative polarization measurements obtained using a standard 30 W fiber-coupled LDA system (Coherent FAP), and from the VHG-narrowed Comet module

employing the polarization-preserving fiber, are given in **Table 1**. Optical spectra of the output from the Coherent FAP and Comet as a function of temperature are shown in **Figure 2**.

We have also begun modification of the polarizer hardware to enable the production of multiple batches of hyperpolarized  $^3\text{He}$ . With a modified cleaning/high-temperature/vacuum treatment procedure of the glass [26] prior to fabrication of the optical pumping cells, we have been able to achieve  $^3\text{He}$  polarization lifetimes ( $T_1$ ) in valved pyrex cells of  $\sim 60$  hours, up from  $\sim 10 - 15$  hours previously. This result not only leads to a  $\sim 30\%$  improvement in the attainable polarization during the SEOP procedure, but potentially allows the gas to be stored for later use while additional batches are polarized. Storage also requires an extremely homogeneous holding field to reduce the effects of polarization loss via diffusion through field gradients. For the 2.3 mT magnetic field in the  $^3\text{He}$  polarizer and a  $^3\text{He}$  diffusion coefficient,  $D = 1.84 \text{ cm}^2/\text{s}$  at 1 bar, transverse field gradients must be minimized to  $< 2.5 \times 10^{-3} \text{ mT/cm}$  in order to achieve a relaxation rate  $> (100 \text{ hr})^{-1}$  [27]. A simple pair of Helmholtz coils of reasonable size does not provide a large enough region of uniform holding field to maintain four storage cells without significant polarization loss. We therefore added an additional coil at the center of our polarizer, in order to increase the region of high field homogeneity  $\sim 6$ -fold [28], large enough to accommodate the SEOP cell and four storage cells. This modification will allow the production of up to 5 batches of hyperpolarized  $^3\text{He}$  over a  $\sim 50$  hr period prior to a single human imaging session, enabling posture dependent studies on the same day, or ventilation imaging from successive breaths of  $^3\text{He}$ .

**MRI Techniques:** Oxygen partial-pressure ( $p\text{O}_2$ ) mapping using  $^3\text{He}$  MRI is accomplished using repeated two-dimensional gradient-recalled echo (FLASH) images, and observing the time-decay of the  $^3\text{He}$  MRI signal [7,8]. For phantom and human studies, 2D images were acquired without

slice selection, using an excitation flip angle of  $\sim 3^\circ$ , data-set size of  $128 \times 32$ ,  $50 \times 50$  cm field of view (FOV) in  $\sim 2$  seconds. All imaging acquisitions used the following parameters: bandwidth = 4.6 kHz, 300  $\mu$ s square RF pulse, TE/TR  $\sim 29/86$  ms, NEX = 1. The datasets were zero-filled to  $128 \times 64$  points before fast-Fourier-transformation. To follow the time-course of the  $^3\text{He}$  magnetization, 3 – 8 images were acquired successively, with 5-second inter-image delays, resulting in experiments ranging from  $\sim 15 - 50$  seconds in duration. Flip angle maps were acquired with an identical procedure, except that the inter-image delay was set to 100 ms.

$p\text{O}_2$  determination is possible due to the effect of molecular  $\text{O}_2$  in greatly reducing  $^3\text{He}$   $T_1$  via an intermolecular dipolar relaxation process. The  $\text{O}_2$ -induced relaxation follows the relationship:  $T_1^{\text{ox}} = 1800 \text{ (torr.s)}/p\text{O}_2 \text{ (torr)}$  [7]. As the typical alveolar oxygen partial pressure,  $p_{\text{A}}\text{O}_2 \sim 90 - 120$  torr in human lungs, we can calculate  $T_1^{\text{ox}} \sim 10 - 15$  s. As the inherent spin-lattice  $T_1$  of  $^3\text{He}$  is of order hours and surface relaxation of order minutes, the observed  $T_1$  of  $^3\text{He}$  in the lung is dominated by oxygen relaxation [7,8]. The method for image-based  $p\text{O}_2$  determination is similar to measurements of hyperpolarized noble gas flip-angle or  $T_1$ , derived from the relationship between the NMR signal from the  $n$ th pulse in a series of pulses,  $\ln(S_n)$ , with the pulse flip angle  $\theta$ , and inter-pulse time  $\tau$  [19]. However, instead of acquiring a series of FIDs, we obtain a series of  $m$  images with  $n$  RF pulses per image, and a time  $\tau$  between each image acquisition (inter-image delay + image acquisition time). The MRI signal relationship can then be written [29]:

$$\ln(S_m/S_0) = nm \ln(\cos \theta) - m \frac{\tau}{T_1^{\text{ox}}} = nm \ln(\cos \theta) - m \frac{\tau \cdot p\text{O}_2}{1800}. \quad [1]$$

Plotting  $\ln(S_m/S_0)$  vs  $m\tau$  on a pixel-by-pixel basis yields lines with slope =  $(n \ln(\cos \theta))/\tau - p\text{O}_2/1800$ , from which  $p\text{O}_2$  can be calculated if  $\theta$  is known. Image-based flip angle calibrations

were performed prior to  $p\text{O}_2$  measurements, in order to calibrate  $\theta$ . The image analysis was identical, except that in the absence of  $\text{O}_2$ , the slope of  $\ln(S_m/S_0)$  vs  $m\tau$  reduces to  $(n \ln(\cos \theta))/\tau$ .

***Human Imaging Protocol:*** After expiration to their lung functional residual capacity ( $\sim 2.5 - 3$  liters for healthy adults), the subjects inhale  $\sim 500 \text{ cm}^3$  of hyperpolarized  $^3\text{He}$  gas, followed by a small breath of air to wash the helium out of the large airways. The MR imaging sequence begins immediately after inhalation, and proceeds during breath-hold for  $\sim 30 - 40$  seconds. All human experiments are performed according to a protocol approved by the Partners Human Research Committee at Brigham and Women’s Hospital, under an inter-institutional IRB agreement with the Harvard University Committee for the Use of Human Subjects in Research.

## RESULTS AND DISCUSSION

**Figure 3** shows an image-based flip-angle calibration conducted using  $\sim 500 \text{ cm}^3$  of hyperpolarized helium expanded into a 2-Liter Tedlar plastic bag which was previously filled with  $\sim 1$  Liter of  $\text{N}_2$ . The bag measures  $\sim 15 \times 15 \text{ cm}$ . Figure 3 a-d) shows 4 of the 8 spin density images acquired during the time-course experiment. The spin-density images are not uniform due to non-uniform mixing of the hyperpolarized  $^3\text{He}$  in the  $\text{N}_2$ , and distortions of the partially-filled bag. As the image acquisition time is finite, the time  $t$  represents the “average” time-point during the experiment at which the image was acquired (i.e., half the image acquisition time of 1.9 s). For this experiment, with an inter-image delay of 100 ms,  $\tau = 2.0 \text{ s}$ . Figure 3e) shows the flip-angle map, and Figure 3f) shows a semi-log plot of signal attenuation vs total experiment time ( $m\tau$ ) from a pixel near the center of the image. Despite the non-uniformity of the spin-density images, the flip-angle is very uniform across the dimensions of the bag,  $\sim 3.9 \pm 0.2^\circ$ . This  $\sim 5\%$  variation matches precise spectroscopy measurements taken at

various positions in this RF coil, and agrees with the standard equations for a RF field in a solenoid coil [17]. Importantly, at the frequency of 210 kHz – below the sample-noise-dominated regime for human MRI, RF coil loading is negligible and thus the above calibration can be used reliably for human experiments, vastly simplifying human  $p_{\text{A}}\text{O}_2$  measurements in comparison to those performed at high-field with clinical scanners [7,8].

We tested the  $p\text{O}_2$  mapping protocol on Tedlar plastic bags with  $p\text{O}_2$  ranging from 50 – 160 torr. **Figure 4a)** shows a  $p\text{O}_2$  map derived from one such experiment. The bag was filled carefully by syringe to contain  $p\text{O}_2 = 68 \pm 5$  torr after the addition of 500 cm<sup>3</sup> of hyperpolarized <sup>3</sup>He. We had previously calibrated  $\theta$ , using the procedure shown in Figure 3, to be 2.3° in this instance, and  $\tau \sim 7$  s (inter-image delay = 5 s). There is some slight variation in  $p\text{O}_2$  throughout the bag, due to imperfect mixing of the gases prior to image acquisition, however the average value obtained across the bag is  $p\text{O}_2 = 60.5 \pm 7$  torr. Individual pixels exhibited  $p\text{O}_2$  ranging from 56 – 70 torr.

An initial human  $p_{\text{A}}\text{O}_2$  map obtained using our open-access imager is shown in **Figure 4b)**. For this trial, the subject was lying horizontally, and the image was obtained in the sagittal orientation, i.e., a transverse cross-section of the lungs. Images acquired in this orientation show the lungs in a gravity-dependent state, i.e., gravitational force is acting down in the plane of the image, however the lung dimensions over which gravity is acting are minimized, and the lungs are constrained by the chest wall. Therefore, there is minimal,  $p_{\text{A}}\text{O}_2$  gradient observed with gravity in this orientation. The average measured  $p_{\text{A}}\text{O}_2$  value throughout the lungs is  $95 \pm 6$  torr, within the expected physiological range of 90 – 120 torr. Our image acquisition protocol of 2 s image time and 5 s inter-image delays allowed the acquisition of 5 – 6 images during the maximum 30 – 40 second breath-hold tolerable for most subjects. By reducing the number of phase encodes and acquisition points, we decrease the overall spatial resolution but boost the

SNR in the later images, at which time the  $^3\text{He}$  polarization has undergone significant  $T_1$  decay. The resulting spatial resolution of  $\sim 0.5 \times 2$  cm is adequate for initial  $p\text{O}_2$  mapping of the lung and detection of gross changes in  $p\text{O}_2$  as a function of posture. In these initial studies, we do not calculate the effect of oxygen uptake from the lungs during the breath-hold. This value is known to be  $\sim 2$  torr/s [7], and in our calculation, its minor effect is included in the error quoted on  $p\text{O}_2$ .

We note the images were acquired without slice selection.  $p_{\text{A}}\text{O}_2$  mapping relies on accurately measuring MRI signal attenuation as a function of time. However, the use of narrow slice-selective imaging methods can lead to reduced accuracy in quantitative data as out-of-slice magnetization diffuses into the image slice during pulse-sequence and inter-image delays. 2D projection methods reduce this effect.

## CONCLUSION

We have demonstrated initial regional measurements of the partial pressure of oxygen,  $p\text{O}_2$ , using hyperpolarized  $^3\text{He}$  and an open-access, very-low-field MRI system operating at 6.5 mT (210 kHz for  $^3\text{He}$ ). Image-based flip-angle measurements have confirmed that the solenoid RF coil exhibits a very homogeneous  $B_1$  field and therefore uniform RF excitation flip angles. At our operating frequency, coil loading is negligible, allowing the use of a single, calibrated flip-angle for human  $p_{\text{A}}\text{O}_2$  measurements without the need to perform a calibration with each measurement and subject. Initial  $p\text{O}_2$  mapping experiments with phantoms validate our procedure, and an initial human  $p_{\text{A}}\text{O}_2$  map yields physiologically expected values. The maps have a resolution of  $\sim 0.5 \times 2$  cm. We have also made significant hardware improvements to our helium polarizer to increase the maximum polarization attainable and the production rate. Our experiments indicate that the open-access imager will enable posture-dependent pulmonary

functional imaging and thereby serve as a valuable tool for the study of critical pulmonary diseases and questions relating to posture-dependent on pulmonary function.

### **ACKNOWLEDGEMENTS**

We are indebted to Kenneth Tsai, MD, who acted as observing physician for human imaging trials, and George Topulos, MD, who devised the human protocols. We are grateful to Rick Frost and the Spectra-Physics division of Newport Corp. for assistance with and trials of novel Comet<sup>TM</sup> VHG-narrowed laser modules. Support is acknowledged from NASA grant NAG9-1489 and NIH grant R21 EB006475-01A1. This material is also based upon work supported by the National Science Foundation under Grant PHY-0618891. Any opinions, findings, and conclusions or recommendations expressed in this material are those of the author(s) and do not necessarily reflect the views of the National Science Foundation.

## REFERENCES

1. T. G. Walker, W. Happer, *Rev. Mod. Phys.* **1997**, *69*, 629-642.
2. P. J. Nacher, M. Leduc, *J. Physique*, **1985**, *46*, 2057-2073.
3. J. C. Leawoods, D. A. Yablonskiy, B. Saam, D. S. Gierada, M. S. Conradi, *Concepts Magn. Reson.* **2001**, *13*, 277-293.
4. H. E. Moller, X. J. Chen, B. Saam, K. D. Hagspiel, G. A. Johnson, T. A. Altes, E. E. de Lange, H.-U. Kauczor, *Magn. Reson. Med.* **2002**, *47*, 1029-1051.
5. J. M. Wild, M. N. J. Paley, L. Kasuboski, A. Swift, S. FICHELE, N. Woodhouse, P. D. Griffiths, E. J. R. van Beek, *Magn. Reson. Med.* **2003**, *49*, 991-997.
6. M. Salerno, E. E. de Lange, T. A. Altes, J. D. Truwit, J. R. Brookeman, J. P. Mugler III, *Radiology*, **2002**, *222*, 252-260.
7. A. J. Deninger, B. Eberle, M. Ebert, T. Grossmann, G. Hanisch, W. Heil, H.-U. Kauczor, K. Markstaller, E. Otten, W. Schreiber, R. Surkau, N. Weiler, *NMR Biomed.* **2000**, *13*, 194-201.
8. R. R. Rizi, J. E. Baumgardner, M. Ishii, Z. Z. Spector, J. M. Edvinsson, A. Jalali, J. Yu, M. Itkin, D. A. Lipson, W. Gefter, *Magn. Reson. Med.* **2004**, *52*, 65-72.
9. G. H. Mills, J. M. Wild, B. Eberle, E. J. Van Beek, *British Journal of Anaesthesia.* **2003**, *91*, 16-30.
10. S. Samee, T. A. Altes, P. Powers, E. E. de Lange, J. Knight-Scott, G. Rakes, J. P. Mugler, J. M. Ciambotti, B. A. Alford, J. R. Brookeman, T. A. E. Platts-Mills, *J. Allergy Clin. Immunol.* **2003**, *111*, 1205-1211.
11. M. Mure, K. B. Domino, S. G. E. Lindahl, M. P. Hlastala, W. A. Altemeier, R. W. Glenny, *J. Appl. Physiol.* **2000**, *88*, 1076-1083.
12. M. Mure, S. G. E. Lindahl, *Acta Anaesthesiol. Scand.* **2001**, *45*, 150-159.
13. L. Gattinoni, G. Tognoni, A. Pesenti, P. Taccone, D. Mascheroni, V. Labarta, R. Malacrida, P. Di Giulio, R. Fumagalli, P. Pelosi, L. Brazzi, R. Latini. *N. Engl. J. Med.* **2001**, *345*, 568-573.

14. G. Musch, J. D. Layfield, R. S. Harris, M. F. Melo, T. Winkler, R. J. Callahan, A. J. Fischman, J. G. Venegas, *J. Appl. Physiol.* **2002**, *93*, 1841-1851.
15. S. Fichele, N. Woodhouse, A. J. Swift, Z. Said, M. N. J. Paley, L. Kasuboski, G. H. Mills, E. J. R. van Beek, J. M. Wild, *J. Magn. Reson. Imaging* **2004**, *20*, 331-335.
16. L. L. Tsai, R. W. Mair, C.-H. Li, M. S. Rosen, S. Patz, R. L. Walsworth, *Acad. Radiol.* **2008**, in press.
17. L. L. Tsai, R. W. Mair, M. S. Rosen, S. Patz, R. L. Walsworth, *J. Magn. Reson.* **2008** submitted.
18. C.-H. Tseng, G. P. Wong, V. R. Pomeroy, R. W. Mair, D. P. Hinton, D. Hoffmann, R. E. Stoner, F. W. Hersman, D. G. Cory, R. L. Walsworth, *Phys. Rev. Lett.* **1998**, *81*, 3785-3788.
19. G. P. Wong, C. H. Tseng, V. R. Pomeroy, R. W. Mair, D. P. Hinton, D. Hoffmann, R. E. Stoner, F. W. Hersman, D. G. Cory, R. L. Walsworth, *J. Magn. Reson.* **1999**, *141*, 217-227.
20. R. W. Mair, M. I. Hrovat, S. Patz, M. S. Rosen, I. C. Ruset, G. P. Topulos, L. L. Tsai, J. P. Butler, F. W. Hersman, R. L. Walsworth. *Magn. Reson. Med.* **2005**, *53*, 745-749.
21. I. C. Ruset, L. L. Tsai, R. W. Mair, S. Patz, M. I. Hrovat, M. S. Rosen, I. Muradian, J. Ng, G. P. Topulos, J. P. Butler, R. L. Walsworth, F. W. Hersman. *Concepts Magn. Reson. B - Magn. Reson. Eng.* **2006**, *29B*, 210-221.
22. P. S. Morgan, S. Conolly, A. Mazovski. *Proc. 5th Scientific Meeting of ISMRM*, Vancouver, Canada, **1997**, *5*, 1447.
23. D. A. Yablonskiy, A. L. Sukstanskii, J. J. H. Ackerman, *J. Magn. Reson.* **2005**, *174*, 279-286.
24. E. Babcock, B. Chann, I. A. Nelson, T. G. Walker, *App. Optics* **2005**, *44*, 3098-3104
25. F. Havermeyer, W. Liu, C. Moser, D. Psaltis and G. J. Steckman, *Opt. Eng.* **2004**, *43*, 2017-2021.
26. R. E. Jacob, S. W. Morgan, B. Saam, *J. Appl. Phys.* **2002**, *92*, 1588-1597.
27. L. D. Schearer, G. K. Walters, *Phys. Rev.* **1965**, *139*, 1398-1402.
28. J. Wang, X. S. She, S. J. Zhang, *Rev. Sci. Instrum.* **2002**, *73*, 2175-2179.

29. L. L. Tsai, PhD thesis, **2006**, Harvard University.

30. A. L. Zook, B. B. Adhyaru, C. R. Bowers, *J. Magn. Reson.* **2002**, *159*, 175-182.

## TABLE

**Table 1.** A comparison of  $^3\text{He}$  NMR signal measurements (arbitrary units) obtained with a broadband 30 W laser diode array (Coherent FAP) and a VHG-narrowed 30 W LDA module (Spectra-Physics Comet<sup>TM</sup>), under a variety of configurations at a cell temperature of 180 °C. The FAP laser employed an optical polarizing beam splitter, which resulted in one or two beams of polarized light, each of  $\sim 14$  W, available for the cell [30]. The Comet<sup>TM</sup> used a polarization preserving fiber. Measurements were made with a cell with  $^3\text{He}$   $T_1$  of  $\sim 12$  hr. The performance of the Comet<sup>TM</sup> relative to the FAP laser will be greater in cells with longer  $T_1$ . Additionally, at higher operating temperatures, which favor faster polarization rates due to a higher density of vaporized Rb, the Comet<sup>TM</sup> will be more likely to achieve full polarization of the Rb vapor, and so be even more effective than the FAP than under current conditions.

Laser	FAP: 1 beam	FAP: 2 beams	Comet: 1 beam
$^3\text{He}$ polarization	$36 \pm 5$	$40 \pm 1$	$47 \pm 1$

## FIGURE CAPTIONS

**Figure 1.** a) A photograph of the open-access human MRI system. The 2 m  $B_0$  coil is denoted by an arrow at the top left of the photograph. The other arrow denotes the 0.55 m  $B_0$  coil. The other circular and grid patterns are the gradient coils, located parallel to the  $B_0$  coils. The entire design is mirrored on the other side. The gap between the two pairs of coils is 80 cm. b) A human subject positioned in the imager for vertical orientation imaging.

**Figure 2.** Optical spectra from the broadband Coherent and VHG-line-narrowed Comet<sup>TM</sup> laser, after transmission through the  $^3\text{He}$  SEOP cell, at ambient and operating temperatures. The locked output from the Comet<sup>TM</sup> laser appears as an intense, narrow peak at 794.7 nm, while the output from the Coherent laser is the broad peak. At 150° C, the Rb vapor absorbs all the laser light from Comet<sup>TM</sup>, but not the Coherent laser.

**Figure 3.** a–d) Time series of  $^3\text{He}$  MR images obtained from a plastic bag phantom containing only  $^3\text{He}$  and  $\text{N}_2$ , in order to determine the excitation flip-angle. The plotted field of view is 50 cm. Every second image from the time series is shown. e) Flip-angle map obtained from analysis of signal attenuation. The scale bar values have units of degrees. Flip-angle  $\sim 3.9 \pm 0.2^\circ$ . f) Signal attenuation analysis for a single pixel in the middle of the bag.

**Figure 4.** a)  $p\text{O}_2$  map obtained from a plastic bag phantom containing  $^3\text{He}$  and  $68 \pm 5$  torr of  $\text{O}_2$ . The MRI method yields an average value throughout the bag of  $60.5 \pm 7$  torr. b)  $p_{\text{A}}\text{O}_2$  map from a human volunteer, lying horizontally in the open-access imager, after inhalation of  $500 \text{ cm}^3$  of hyperpolarized  $^3\text{He}$ . In this sagittal orientation, there is little variation in  $p_{\text{A}}\text{O}_2$  across the lungs. The average value is  $95 \pm 6$  torr, close to the physiologically expected value of  $\sim 90 - 120$  torr. The scale bar values for both images have units of torr.



**Figure 1**

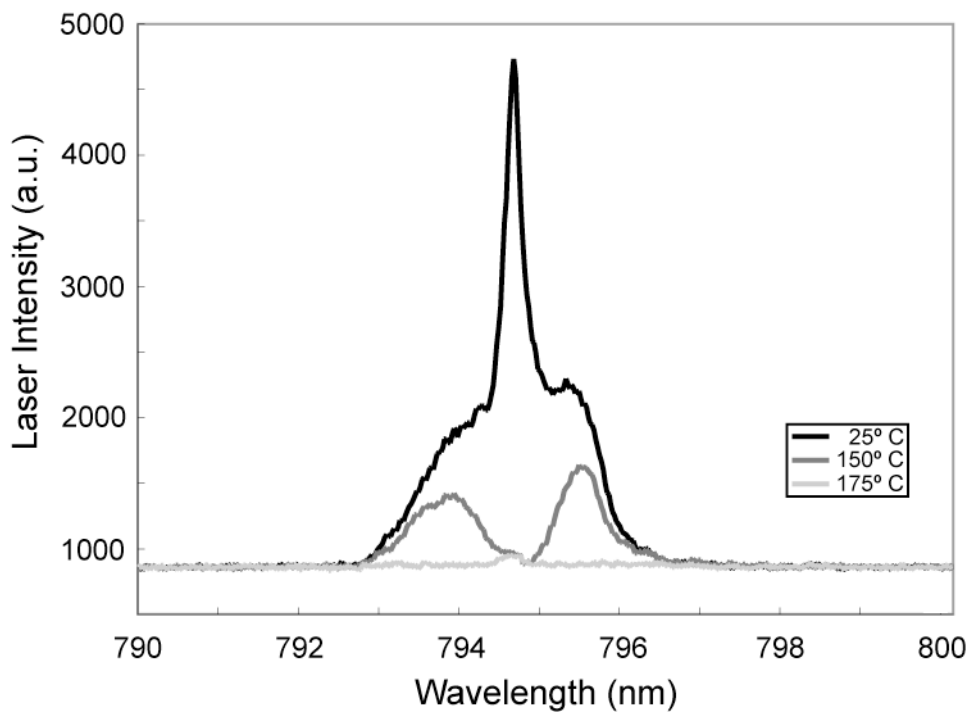


**Figure 2**

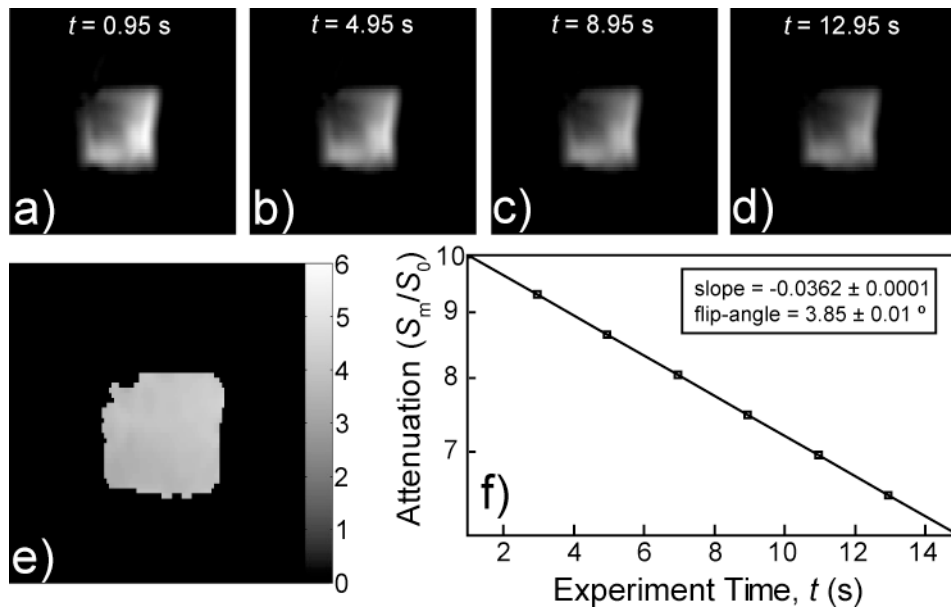


**Figure 3**

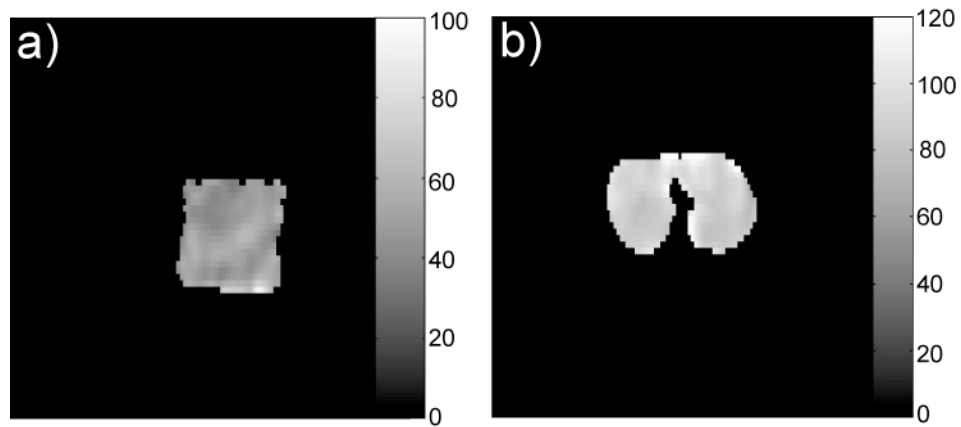


**Figure 4**